A SAR Multiple RFI Suppression Method via Frobenius Norm and Iterative Matrix Decomposition

Qiang Guo, Yuhang Tian, Liangang Qi, Yani Wang, Daren Li, and Mykola Kaliuzhnyi

***Abstract*—The scarcity and sharing nature of the electromagnetic spectrum present a significant challenge to the stable operation of synthetic aperture radar (SAR) systems, as they are susceptible to interference from other devices operating in the same frequency band, known as radio-frequency interference (RFI). In this article, we propose an effective semiparametric method for suppressing multiple RFI, named the iterative matrix decomposition algorithm based on the Frobenius norm (FIMD), we employ CUR decomposition and a soft-threshold algorithm to update low-rank and sparse matrices within an alternate projection framework. It is observed that there exist distinct distribution characteristics between interference points and strong scattering points in the echo domain. We propose a novel and effective signal protection method, which effectively mitigates the risk of strong scattering points being misidentified as interference signals and subsequently eliminated. In addition, we utilize random singular value decomposition instead of traditional singular value decomposition to enhance convergence speed of. Simulation results demonstrate that our proposed method exhibits superior suppression capability and robustness under varying-to-interference ratio conditions and it can be applied to L0-raw products and L1-SLC products.**

***Index Terms*—CUR matrix decomposition, frobenius norm (F-norm), multiple radio-frequency interference (RFI), synthetic aperture radar (SAR).**

I. Introduction

With the rapid advancement of modern communication technology, there has been a continuous increase in spectrum-dependent equipment, leading to an escalating congestion of wireless channels. During surveying and mapping, synthetic aperture radar (SAR) inevitably encounters radio-frequency interference (RFI), wherein signals from other wireless devices within the same frequency band are received. This interference manifests as electromagnetic rain, fog, stripes, and other artifacts on the SAR image, posing significant threats to the SAR imaging system by causing damage to target objects and impairing subsequent image interpretation.

In recent years, numerous scholars have studied the suppression of RFI in SAR, which can be broadly categorized into the following three groups: nonparametric methods, parametric methods, and semiparametric methods.

The nonparametric method involves searching for the transformation domain that exhibits the largest disparity between RFI and useful signal characteristics, in order to design corresponding filters for interference removal. These include enhanced time-frequency filtering methods [1], [2], [3], and notch filtering techniques [4], [5], among others. In the transform domain, a pair of detection thresholds is set to distinguish pulse by pulse, enabling identification and subsequent processing of pulses containing interference using a notch filter. However, the presence of wideband interference (WBI) can result in an elevation of target sidelobes, leading to a substantial degradation in the quality of useful signals. Eigensubspace filtering [6] has been devised by scholars to effectively eliminate narrowband interference (NBI) and account for the statistical disparity in useful echo signals. The three-step operation of block subspace filter (BSF) [7], feature decomposition, and subspace projection, achieves the suppression of RFI. A sub-band cancellation method for narrowband RFI is proposed based on the energy difference between the sub-band containing RFI and the clean sub-band [8]. Building upon this approach, a cancellation method capable of suppressing narrowband and wideband RFI is devised by employing continuous cancellation and data accumulation methods [9]. The 2-D spectral analysis [10] method can be used to suppress linear frequency modulation (LFM) interference signals directly on SLC data. And the nonparametric methods have been widely used in a large number of SAR products due to their ability to quickly and real-time process RFI. In 2022, robust frequency-domain notch filtering (FNF) and notch filtering methods were integrated into S1-IPF. Previously, FNF methods were also used in E-SAR and PALSAR systems due to their excellent performance. While these algorithms possess low complexity and can meet real-time processing requirements, they are only applicable to signals with narrowband and stable interference frequency bands.

The parameterization method assumes that RFI can be represented as the superposition of a series of sinusoidal signals [11] or LFM signals. Modeling is performed by estimating the parameters of the interference signals, and interference suppression is achieved through subtraction with echo signals. In other words,

Manuscript received 27 September 2023; revised 7 December 2023 and 16 January 2024; accepted 17 January 2024. Date of publication 23 January 2024; date of current version 2 February 2024. This work was supported in part by the National Natural Science Foundation of China under Grant 62071140, in part by the National Major Research and Development project of China under Grant 2018YFE0206500, and in part by the Fundamental Research Funds for the Central Universities under Grant 3072022CF0801. *(Corresponding author: Yuhang Tian.)*

Qiang Guo, Yuhang Tian, Liangang Qi, Yani Wang, and Daren Li are with the College of Information and Communication Engineering, Harbin Engineering University, Harbin 150001, China (e-mail: guoqiang@hrbeu.edu.cn; tianyuhang01@hrbeu.edu.cn; qiliangang@hrbeu.edu.cn; 178655165@hrbeu.edu.cn; lidaren@hrbeu.edu.cn).

Mykola Kaliuzhnyi is with the Problem Research Laboratory for Radio Monitoring and Processing of Radio Information, Kharkiv National University of Radio Electronics, 61166 Kharkiv, Ukraine (e-mail: knm1204@ukr.net).

Digital Object Identifier 10.1109/JSTARS.2024.3357131

the effectiveness of RFI elimination depends on the accuracy of parameter estimation. Some scholars have applied statistical methods in this field, such as the least square method [12] and improved minimum mean square error [13]. Zhou et al. [14] decomposed the echo containing NBI into eigenmode functions using complex empirical mode decomposition and completed suppression in the echo domain through thresholding. The U.S. Army Research Laboratory has conducted extensive research on RFI suppression, designed a satellite-based P-band RFI filter [15], and developed a new system to improve parameter estimation accuracy using modern spectrum estimation theory, which has been extended to broadband interference suppression. Despite the utilization of parameterization method in practical SAR systems, accurately estimating parameters and modeling interference sources remains a significant challenge due to the diverse nature and frequency time variability of interference in complex electromagnetic environments.

The semiparametric method transforms the problem of signal separation in sparse signal theory and low-rank decomposition theory into hyperparameter optimization during iterative optimization. And it is a hybrid approach that combines nonparametric and parametric methods, leveraging SAR echo characteristics for processing while incorporating parameter estimation based on prior knowledge. The proposed method generally outperforms nonparametric approaches and exhibits broader applicability compared to parametric methods. For the sparse recovery of useful signals, atomic norm proposed by Liu et al. [16] and Bayesian learning proposed by Lu et al. [17] are employed to enhance the accuracy of estimating sparse signals, while sparse Bayesian inference and prior RFI spatial distribution [18] are utilized for RFI detection and suppression. In the context of sparse low-rank recovery methods, Su et al. [19] initially applied robust principal component analysis to the domain of SAR interference suppression. Within this framework, Yang et al.[20] employed a dictionary-based representation to effectively attenuate NBI caused by sparse echoes. In recent years, Huang has proposed a series of semiparametric techniques including alternating projection [21], matrix factorization [22], parameter free decomposition [23], and tensor decomposition [24], [25], which have yielded promising outcomes. The semiparametric method should be noted as an iterative optimization algorithm, which inevitably involves complex operations like matrix decomposition when solving low-rank matrices. Improper selection of hyperparameters not only leads to slow convergence speed but also affects the inhibitory effect of the algorithm. In comparison with nonparametric methods, semiparametric methods are more suitable for offline processing.

Previous approaches have focused on considering the disparity in power or energy levels between useful signals and interference, employing techniques, such as transform domain suppression or sequential projection of echo data into subspaces to suppression RFI. However, these methods did not take into account the distribution differences between RFI and useful signals in the echo matrix. In addition, in actual SAR applications, users are using more L1-SLC products rather than L0-raw products. This makes most of the abovementioned methods for processing in the echo domain ineffective. Based on the abovementioned reasons, we propose an iterative matrix factorization algorithm based on Frobenius norm (F-norm) within the framework of alternating projection, and it can be applied to L0-raw products and L1-SLC products. This algorithm involves sampling the most relevant rows and columns of the matrix, thereby constructing a compact and effective approximation matrix with low rank to approach the original echo matrix. The main contributions are as follows.

1) We propose a novel semiparametric interference suppression algorithm that combines CUR decomposition with alternating projection. During the iteration, we sequentially employ CUR decomposition to update the low-rank matrix and utilize a soft-threshold algorithm to update the sparse matrix.
2) Based on the different distribution characteristics of interference signals and useful signals in the echo domain, the weight factor of F-norm is designed to address the issue of useful signal elimination due to the overlap of interference signals and strong scattering points in the echo domain, thereby safeguarding the integrity of the useful signal.
3) In the face of large-scale echo matrices, random singular value decomposition (RSVD) is used instead of the singular value decomposition (SVD) algorithm to accelerate the convergence of the algorithm.

The rest of this article is organized as follows. Section II presents the signal model of RFI in complex electromagnetic environments, along with the "sparse + low rank" RFI decomposition model. Section III provides a comprehensive explanation of the FIMD method, encompassing the design of F-norm weights factors and the iterative update process for both RFI and useful signal components. Section IV provides two experiments, real echo data superimposed with simulated interference and SLC with real interference, for comparison with existing methods and numerical analysis. Section V critically examines the advantages and disadvantages of the FIMD algorithm, while also outlining future directions for research. Finally, Section VI concludes this article.

II. Signal Model

The signals are arranged in a two-dimensional matrix based on the azimuth direction of SAR motion and the range direction of the radar beam. The echo signal of SAR can be described as follows:

$$\boldsymbol{Y}(\tau,\eta)=\boldsymbol{S_0}(\tau,\eta)+\boldsymbol{L}(\tau,\eta)+\boldsymbol{N}(\tau,\eta) \tag{1}$$

where τ represents the fast time in range direction, η represents the slow time in azimuth direction, $\boldsymbol{S_0}$, $\boldsymbol{L}$, and $\boldsymbol{N}$ represent the useful echo signal, RFI and noise, respectively. The objective of our study is to extract the RFI component from the mixed echo data, aiming to achieve effective suppression of RFI and facilitate subsequent analysis. Therefore, (1) can be abbreviated as

$$\boldsymbol{Y}(\tau,\eta)=\boldsymbol{S}(\tau,\eta)+\boldsymbol{L}(\tau,\eta) \tag{2}$$

where $\boldsymbol{S}$ contains useful signal $\boldsymbol{S_0}$ and noise $\boldsymbol{N}$. Generally, the multiple RFI (MRFI) encompasses both NBI and WBI.

The NBI was defined as RFI accounting for 1% or less of the SAR bandwidth [26]. The NBI including amplitude modulation, frequency modulation, and phase modulation. Its mathematical model is represented as follows:

$$\boldsymbol{L}_{\mathrm{NBI}}(\tau,\eta)=\sum_{i=1}^{k}U_i(\tau,\eta)(\exp(j2\pi f_{\mathrm{NBI}}\tau+\varphi_i(\tau,\eta)) \tag{3}$$

where k represents the number of RFI signals, the envelope function $U_i(\tau,\eta)$ follows rayleigh distribution to represent the amplitude of the ith pulse, f_{NBI} represents the carrier frequency of NBI, $\varphi_i(\tau,\eta)$ follows uniform distribution to represent the phase of the ith pulse.

In order to closely simulate real interference scenarios, we employ commonly utilized phase-shift keying (2PSK) signals in communication, LFM signals transmitted by C-band pulse Doppler radar, and sinusoidal frequency modulation (SFM) signals transmitted by frequency modulated continuous wave radar to emulate broadband interference signals. The mathematical model can be represented as

$$\begin{aligned}\boldsymbol{L}_{\mathrm{WBI}}(\tau,\eta)=\sum_{i=1}^{k}U_i(\tau,\eta)\{&\cos(\omega\tau+\varphi_1)\\&+\exp\left(j2\pi f_{\mathrm{LFM}}\tau+j\pi K\tau^2\right)\\&+\exp(j\sin(2\pi f_{\mathrm{SFM}}\tau+\varphi_2)\}\end{aligned} \tag{4}$$

where ω and φ_1 represent the frequency and phase of the 2PSK signal, respectively. f_{LFM} represents the frequency of the LFM signal, and K represents the chirp rate of wideband LFM interference. And f_{SFM}, φ_2 represents the frequency and phase of the SFM signal.

The problem of RFI suppression can be formulated as the separation of a low-rank RFI matrix and a sparse useful echo matrix from the original echo data, which is solved by the following optimization:

$$\begin{aligned}&\min_{\boldsymbol{L},\boldsymbol{S}}\operatorname{rank}(\boldsymbol{L})+\lambda\|\boldsymbol{S}\|_0\\&\text{s.t. }\|\boldsymbol{Y}-\boldsymbol{L}-\boldsymbol{S}\|_F^2<\delta\end{aligned} \tag{5}$$

where rank(•) is the rank operation, $\|\bullet\|_0$ stands for the l_0 norm, $\|\bullet\|_F$ stands for the F-norm, λ is the sparsity control constant, which is generally $\lambda=1/\sqrt{\max(\mathrm{row},\mathrm{col})}$, and row, col are the rows and columns of the matrix $\boldsymbol{S}$, $\delta=10^{-6}$ is the loss factor. The abovementioned formula, however, poses an NP-hard problem and cannot be directly solved. Some studies [27], [28] have proposed a relaxation of (5) by substituting rank(•) with the nuclear norm. By replacing the l_0 norm with the l_1 norm, (5) can be reformulated as follows:

$$\begin{aligned}&\min_{\boldsymbol{L},\boldsymbol{S}}\|\boldsymbol{L}\|_*+\lambda\|\boldsymbol{S}\|_1\\&\text{s.t. }\|\boldsymbol{Y}-\boldsymbol{L}-\boldsymbol{S}\|_F^2<\delta\end{aligned} \tag{6}$$

where the nuclear norm $\|\boldsymbol{L}\|_*=\sum_i\sigma_i(\boldsymbol{L})$ represents the sum of the singular values of the matrix $\boldsymbol{L}$, and the l_1 norm is represented as $\|\boldsymbol{S}\|_1=\max_j\sum_{i=1}^{m}|a_{i,j}|$. Equation (6) is a convex problem, and algorithms, such as lagrange multiplier method [29] and alternating direction multiplier method [21], are used to iteratively optimize the subproblem to solve the low-rank matrix $\boldsymbol{L}$ and the sparse matrix $\boldsymbol{S}$. However, the application of the SVT algorithm in low-rank matrix resolution leads to excessive penalization of large singular values [30]. Moreover, the SVD step within the SVT algorithm exhibits high sensitivity toward outliers, specifically strong scattering points in echo data may be compromised during RFI separation, thereby impacting subsequent image interpretation and other related operations. Hence, employing the SVT algorithm for optimizing the kernel function to suppress RFI may not be an optimal approach. Alternatively, considering a priori knowledge of the rank of the low-rank matrix and sparsity of the sparse matrix, we minimize decomposition error while constraining rank and sparsity

$$\begin{aligned}&\min_{\boldsymbol{L},\boldsymbol{S}}\|\boldsymbol{Y}-\boldsymbol{L}-\boldsymbol{S}\|_F^2\\&\text{s.t.}\operatorname{rank}(\boldsymbol{L})\le r\\&\|\boldsymbol{S}\|_0\le\alpha\end{aligned} \tag{7}$$

where r is the rank of the constraint matrix $\boldsymbol{L}$, α represents the sparsity of the matrix $\boldsymbol{S}$, and the two parameters can be set based on prior knowledge. In the iterative process, (6) decomposed into two subproblems to solve, the low-rank matrix and the sparse matrix are successively updated by alternate projection until convergence. This separates the RFI from the raw echo data

$$\begin{aligned}\boldsymbol{L}^{(\mathrm{t}+1)}&=\arg\min_{\boldsymbol{L}}\left\|\boldsymbol{Y}-\boldsymbol{L}^{(\mathrm{t})}-\boldsymbol{S}^{(\mathrm{t})}\right\|_{\mathrm{F}}^2\\&\text{s.t. }\operatorname{rank}(\boldsymbol{L})\le\mathrm{r}\end{aligned} \tag{8}$$

$$\begin{aligned}\boldsymbol{S}^{(t+1)}&=\arg\min_{\boldsymbol{S}}\left\|\boldsymbol{Y}-\boldsymbol{L}^{(t+1)}-\boldsymbol{S}^{(t)}\right\|_F^2\\&\text{s.t.}\|\boldsymbol{S}\|_0\le\alpha(m\times n).\end{aligned} \tag{9}$$

III. Proposed Algorithm

In this section, we propose an iterative matrix decomposition algorithm based on the F-norm to effectively suppress RFI. First, weight factors are designed using the F-norm during the construction of a row subset to mitigate the issue of missing useful signals during random extraction. Second, we employ CUR decomposition technology [31] to update the low-rank matrix $\boldsymbol{L}$ and utilize a soft-threshold algorithm for updating the sparse matrix $\boldsymbol{S}$. Finally, on the premise of ensuring data sparsity and interpretability [32], through iterative update under termination conditions, the extracted low-rank matrix and sparse matrix were refined while the original matrix was approximately reconstructed in each iteration. The flowchart of the proposed algorithms is illustrated in Fig. 1, and the CUR decomposition theory is provided as follows.

Theorem 1: Let $\boldsymbol{Y}\in\mathbb{K}^{m\times n}$ and $\operatorname{rank}(\boldsymbol{Y})=k$, I, J are the index of rows and columns, $I\subset[m]$, $J\subset[n]$ and $|I|,|J|\ge k$. Let $\boldsymbol{C}=\boldsymbol{Y}(:,J)$, $\boldsymbol{R}=\boldsymbol{Y}(I,:)$, $\boldsymbol{U}=\boldsymbol{Y}(I,J)$. If $\operatorname{rank}(\boldsymbol{U})=\operatorname{rank}(\boldsymbol{Y})$, then $\boldsymbol{Y}=\boldsymbol{C}\boldsymbol{U}^{\dagger}\boldsymbol{R}$, where $(\bullet)^{\dagger}$ denotes the Moore–Penrose pseudoinverse.

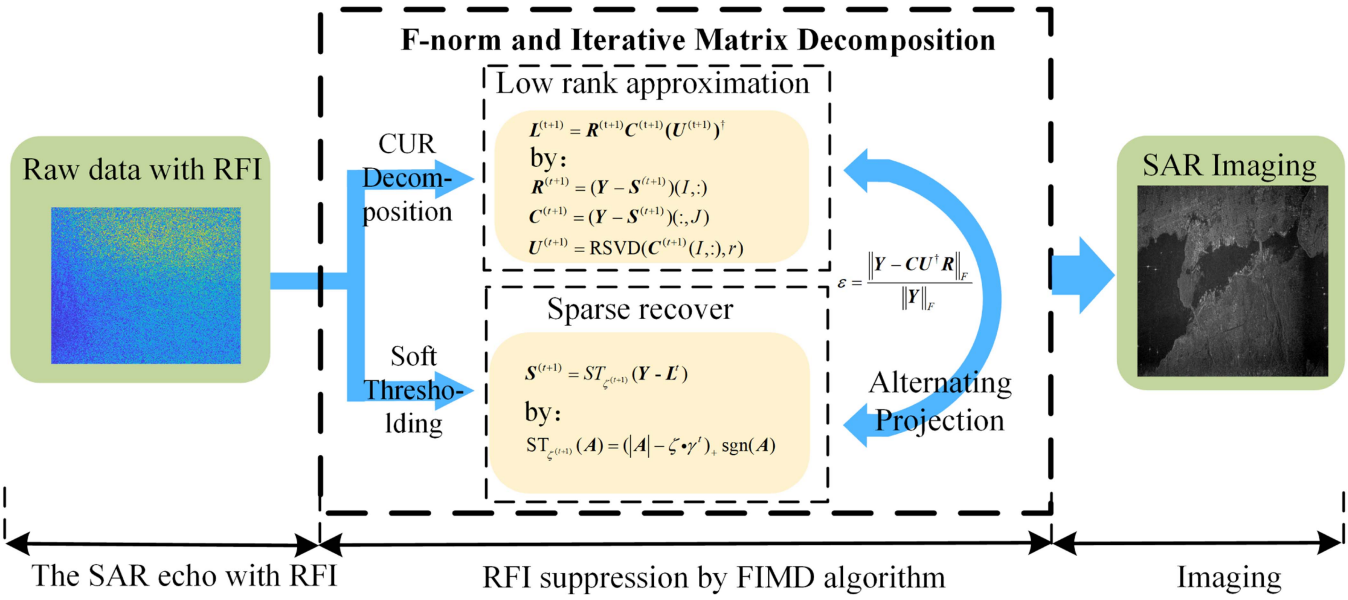

Fig. 1. Flowchart of the proposed algorithm combined with SAR imaging process.

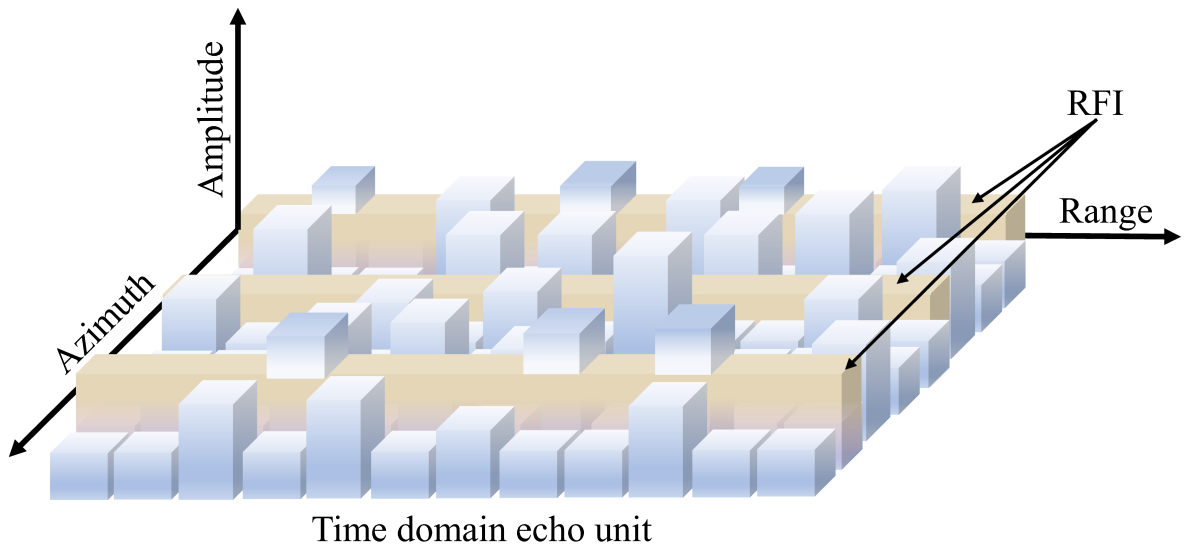

Fig. 2. Schematic diagram of RFI and scatterers distribution in SAR echo domain.

Proof [33]: Given the constraint $\mathrm{rank}(\boldsymbol{U}) = \mathrm{rank}(\boldsymbol{Y})$, it follows that $\mathrm{rank}(\boldsymbol{C}) = \mathrm{rank}(\boldsymbol{R}) = \mathrm{rank}(\boldsymbol{Y})$; thus, there exists a matrix $\boldsymbol{X} \in \mathbb{K}^{s\times n}$ such that $\boldsymbol{Y} = \boldsymbol{C}\boldsymbol{X}$. Let P_I denote the matrix selected from $\boldsymbol{Y}$ based on index set I, then $P_I = \boldsymbol{R}$. Similarly, $P_I\boldsymbol{C} = \boldsymbol{U}$; consequently, $P_I\boldsymbol{Y} = P_I\boldsymbol{C}\boldsymbol{X}$ and subsequently $\boldsymbol{R} = \boldsymbol{U}\boldsymbol{X}$, then $\boldsymbol{X} = \boldsymbol{U}\boldsymbol{R}$, that is, $\boldsymbol{Y} = \boldsymbol{C}\boldsymbol{U}^{\dagger}\boldsymbol{R}$.

Theorem 1 demonstrates that the CUR decomposition of the echo matrix $\boldsymbol{Y}$ in the tth iteration yields a subset $\boldsymbol{C}$ consisting of its J columns, a subset $\boldsymbol{R}$ consisting of its I rows, and their mixing submatrix $\boldsymbol{U}$. In other words, by combining the linear mappings of column space $\boldsymbol{C}$ and row space $\boldsymbol{R}$, it becomes possible to approximately restore a low-rank matrix $\boldsymbol{L}$.

The algorithm can be expressed as: $\boldsymbol{Y} - \boldsymbol{L}^{(t)}$ is successively projected to the useful signal subspace composed of sparse matrix $\boldsymbol{S}$ in the iteration, $\boldsymbol{S}^{(t+1)}$ updated using the soft-threshold algorithm [solution (9)], $\boldsymbol{Y} - \boldsymbol{S}^{(t+1)}$ is projected to the RFI subspace composed of low-rank matrix $\boldsymbol{L}$, and $\boldsymbol{L}^{(t+1)}$ is updated using the CUR matrix decomposition [solution (8)]. The algorithm is described in detail in the following three sections.

A. Range/Azimuth Subset Construction

There exist disparities in the distribution characteristics between interference signals and strong scattering points within the echo domain. If SAR echoes encounter RFI in a fast time, the snapshot will be contaminated by RFI; while strong scattering points are usually isolated, as depicted in Fig. 2. The rows of the specified echo matrix represent the range dimension,

while the columns correspond to the azimuth dimension in this study. We hypothesize that the range dimension data of ith row and the azimuth dimension data of jth column are affected by RFI. Therefore, we utilize the F-norm weights of ith row and jth column for selection when constructing range subset and azimuth subset, instead of employing random sampling [34]. This approach prioritizes minimizing reconstruction errors in the echo matrix at the expense of slightly increased running time, thereby enhancing interference suppression. Consequently, if a certain snapshot is contaminated with RFI, its weight factor becomes higher, increasing its likelihood of being selected. Initially, we compute the weight factor for the ith row of the matrix $\boldsymbol{Y} \in \mathbb{R}^{m\times n}$ range dimension

$$W_i = \sum_{j=1}^{n} {y_{ij}}^2. \tag{10}$$

Similarly, we define the weight factor of the jth column of the azimuth dimension as

$$cW_j = \sum_{i=1}^{m} {y_{ij}}^2. \tag{11}$$

The weight factor obtained by (10) and (11) is also equal to the square of the F-norm of the respective row/column. We utilize the ratio of F-norms to determine the probability of each row/column being sampled for constructing range subset $\boldsymbol{R} \in \mathbb{R}^{i\times n}$, and azimuth subset $\boldsymbol{C} \in \mathbb{R}^{\mathrm{m}\times j}$

$$P_i = \frac{W_i}{\|\boldsymbol{Y}\|_F^2}, P_j = \frac{W_j}{\|\boldsymbol{Y}\|_F^2}. \tag{12}$$

The sampling probabilities derived from (12) are arranged in descending order. Rows corresponding to the first I weight factors are selected to construct the matrix $\boldsymbol{R} = \boldsymbol{Y}(I,:)$, which serves as the range subset matrix. Similarly, column J is extracted from matrix $\boldsymbol{Y}$ to form the azimuth subset matrix $\boldsymbol{C} = \boldsymbol{Y}(:,J)$.

B. Update Sparse Matrix $\boldsymbol{S}$

In contrast to image detection and foreground–background separation, which involve processing real data, SAR echo data is represented as a two-dimensional complex matrix. The soft-threshold algorithm is preferred over the hard threshold algorithm due to its ability to mitigate additional reconstruction errors associated with complex data processing and expedite algorithm convergence [35]. Consequently, the soft-threshold algorithm is employed for solving (9) to update the sparse matrix, where ζ denotes the initial threshold and γ represents the threshold attenuation parameter

$$\boldsymbol{S}^{(t+1)} = ST_{\zeta^{(t+1)}}(\boldsymbol{Y} - \boldsymbol{L}^t) \tag{13}$$

where

$$ST_{\zeta^{(t+1)}}(\boldsymbol{A}) = \left(|\boldsymbol{A}| - \zeta\cdot\gamma^t\right)_+ \operatorname{sgn}(\boldsymbol{A}). \tag{14}$$

C. Update Low-Rank Matrix $\boldsymbol{L}$

For the $t+1$ iteration, the CUR decomposition is adopted to update the low-rank matrix $\boldsymbol{L}$, and (8) can be expressed as

$$\boldsymbol{L}^{(t+1)} = \boldsymbol{R}^{(t+1)}\boldsymbol{C}^{(t+1)}({\boldsymbol{U}^{(t+1)}}^{\dagger} \tag{15}$$

Algorithm 1: Proposed Algorithm FIMD.

INPUT : $\boldsymbol{Y}$:echo matrix; r:rank; ζ:initial threshold;
γ:attenuation parameters;
Initialize:$t=0, L^0=0, S^0=0, \varepsilon^0=10^{-6}$
while $\varepsilon^t \geqslant \varepsilon^0$ **do**
  // Constructing row/column subsets
  for $i = 1,\ldots,row/col$ **do**
    Calculate P_i/P_j via (12)
    //Descending arrangement P_i/P_j
    $\boldsymbol{R}^{(t+1)} = \boldsymbol{Y}^{(t+1)}(I,:)$; $\boldsymbol{C}^{(t+1)} = \boldsymbol{Y}^{(t+1)}(:,J)$
  end for
  //Update spare matrix
  $\zeta^{(t+1)} = \zeta^t \times \gamma$
  Update $\boldsymbol{S}^{(t+1)}$ via (13)
  //Update low rank matrix
  Update $\boldsymbol{R}^{(t+1)}, \boldsymbol{C}^{(t+1)}, \boldsymbol{U}^{(t+1)}$ via (16)–(18)
  Update $\boldsymbol{L}^{(t+1)}$ via (15)
  $t \leftarrow t+1$
end while
OUTPUT: $\boldsymbol{L}$, $\boldsymbol{S}$;

where $\boldsymbol{R}^{(t+1)}$ and $\boldsymbol{C}^{(t+1)}$ are updated by the sampling probability P_i, P_j calculated by the $\boldsymbol{Y} - \boldsymbol{S}^{(t+1)}$ matrix according to (12)

$$\boldsymbol{R}^{(t+1)} = (\boldsymbol{Y} - \boldsymbol{S}^{(t+1)})(I,:) \tag{16}$$

$$\boldsymbol{C}^{(t+1)} = (\boldsymbol{Y} - \boldsymbol{S}^{(t+1)})(:,J). \tag{17}$$

The RSVD algorithm is employed to update $(\boldsymbol{U}^{(t+1)})^{\dagger}$ in order to achieve rapid convergence. RSVD essentially extends feature decomposition to large-scale matrices. First, the mixing submatrix $\boldsymbol{U} = (\boldsymbol{C}^{(t+1)})(I,:)$ or $\boldsymbol{U} = (\boldsymbol{R}^{(t+1)})(:,J)$ is screened out based on the index, and subsequently projected onto the subspace of predicted low-rank r using random sampling techniques for data dimensionality reduction. This reduces computational requirements for subsequent data processing. Moreover, the RSVD algorithm only retains a small portion of randomly sampled space during calculations and does not necessitate storing the complete mixing submatrix $\boldsymbol{U}$, thereby saving memory and reducing storage costs. Moreover, the mixing submatrix $\boldsymbol{U}$ is represented by

$$\boldsymbol{U}^{(t+1)} = \mathrm{RSVD}(\boldsymbol{C}^{(t+1)}(I,:), r) \tag{18}$$

where

$$\mathrm{RSVD}(\boldsymbol{A},r) = \begin{cases} \boldsymbol{A}^{m\times n}\boldsymbol{\Omega}^{n\times r} = \boldsymbol{Y}^{m\times r} \\ \boldsymbol{Y} = \boldsymbol{Q}^{m\times r}\boldsymbol{R}^{r\times r}(QR-\text{ decomposition}) \\ \boldsymbol{Q}^{\mathrm{T}}\boldsymbol{A} = \boldsymbol{B} \\ \boldsymbol{B} = \boldsymbol{U}_B\sum\boldsymbol{V}_B^{\mathrm{T}}(\text{SVD}-\text{ decomposition}) \\ \approx \boldsymbol{Q}\boldsymbol{U}_B\sum\boldsymbol{V}_B^{\mathrm{T}} \end{cases} \tag{19}$$

where $\boldsymbol{\Omega}$ is a random Gaussian matrix. The approximate reconstruction error after iteration is calculated and the termination condition is derived

$$\varepsilon = \frac{\left\|\boldsymbol{Y} - \boldsymbol{C}\boldsymbol{U}^{\dagger}\boldsymbol{R}\right\|_F}{\|\boldsymbol{Y}\|_F}. \tag{20}$$

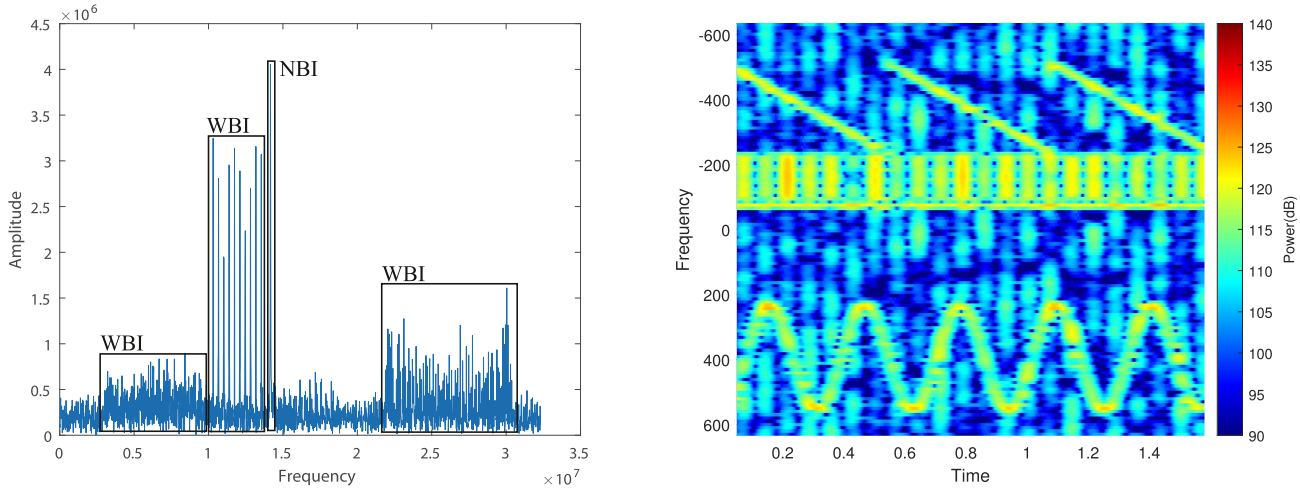

(a) (b)

Fig. 3. SAR echoes contaminated by RFI are observed within distinct domain. (a) Range frequency domain. (b) Range time-frequency domain.

TABLE I
DESCRIPTION OF RADARSAT-1 PARTIAL PARAMETERS

Parameter	Value
Orbital altitude	796 km
Sampling rate	32.317 MHz
Signal bandwidth	30.111 MHz
Pulsewidth	41.74 μs
Radar carrier frequency	5.3GHz (C-band)
Pulse repetition frequency	1256.98 Hz
Radar flight rate	7062 m/s

The FIMD algorithm is summarized in Algorithm 1, and the algorithm analysis and numerical experiments will be carried out in Section IV.

IV. EXPERIMENTAL VERIFICATION

A. Real SAR Echo Data Mixed Simulation Interference

In this section, we validate the efficacy and robustness of the proposed algorithm by superimposing simulated interference on real SAR echo data. We compare the following three metrics: recovery signal to interference ratio (RSIR) [7], structural similarity (SSIM) [36], and running time with GoDec [37], MFD [22], and RTD-BRP [23] algorithms to showcase the advantages of our approach. The SAR echo data used in this study is obtained from the RadarSat-1 satellite launched by Canada. Table I presents key parameters of the spaceborne SAR.

To achieve a more realistic approach to the complex electromagnetic environment, we conducted simulations of MRFI consisting of WBI and NBI. The sampling rate for both SAR radar and interference signals was set at 32.317 MHz. WBI was modulated using LFM, 2PSK, and SFM signals, while NBI used sinusoidal modulation. Specific settings for simulating interferences are presented in the following table.

The clean SAR echo data is combined with the interferences, and then subjected to Fourier transform in the single range dimension. As shown in Fig. 3, it is evident that the single snapshot echo data encompasses different quantities and types of NBI and WBI interference signals.

The RSIR is employed as an evaluation metric to quantify the energy ratio between the real echo image without interference $\boldsymbol{X}$ and the image recovered after suppressing residual interference $\hat{\boldsymbol{X}}$. The higher the RSIR, the cleaner the RFI rejection and the stronger the suppression ability of the algorithm

$$\mathrm{RSIR} = 10\log_{10}\left(\frac{\|\boldsymbol{X}\|_{\mathrm{F}}^2}{\|\boldsymbol{X}-\hat{\boldsymbol{X}}\|_{\mathrm{F}}^2}\right). \tag{21}$$

The SSIM metric is utilized to quantitatively assess the similarity and distortion between the suppressed restored image and the real echo image. A higher SSIM value indicates a stronger resemblance of the suppressed restored image to the original, thereby implying an improved suppression effect. In addition, by extracting and representing weighted features related to brightness, contrast, and structure before and after suppression

$$\mathrm{SSIM}(\boldsymbol{X},\hat{\boldsymbol{X}}) = \frac{(2\mu_x\mu_{\hat{x}}+\varepsilon_1)(2\sigma_{x\cdot\hat{x}}+\varepsilon_2)}{(\mu_x^2+\mu_{\hat{x}}^2+\varepsilon_1)(\sigma_x^2+\sigma_{\hat{x}}^2+\varepsilon_2)} \tag{22}$$

where μ_x and σ_x represent the mean and standard deviation of the real image, while $\mu_{\hat{x}}$ and $\sigma_{\hat{x}}$ denote the mean and standard deviation of the suppressed restored image. $\sigma_{x\cdot\hat{x}}$ represents the covariance between these two images. To assess result stability, positive constants ε_1 and ε_2 are set to 0.01.

In the subsequent analysis, advanced imaging algorithms are employed to visualize the data contaminated with interference at varying SIR, and the resulting images correspond to Fig. 4(a), (f), and (k). Similarly, the GoDec, MFD, RTD-BRP, and our proposed algorithm were applied for RFI suppression. From Fig. 4, it is evident that all four algorithms effectively suppress RFI while recovering the original image to different extents. The outcomes demonstrate that GoDec, MFD, and RTD-BRP algorithms exhibit varying degrees of residual RFI, indicating

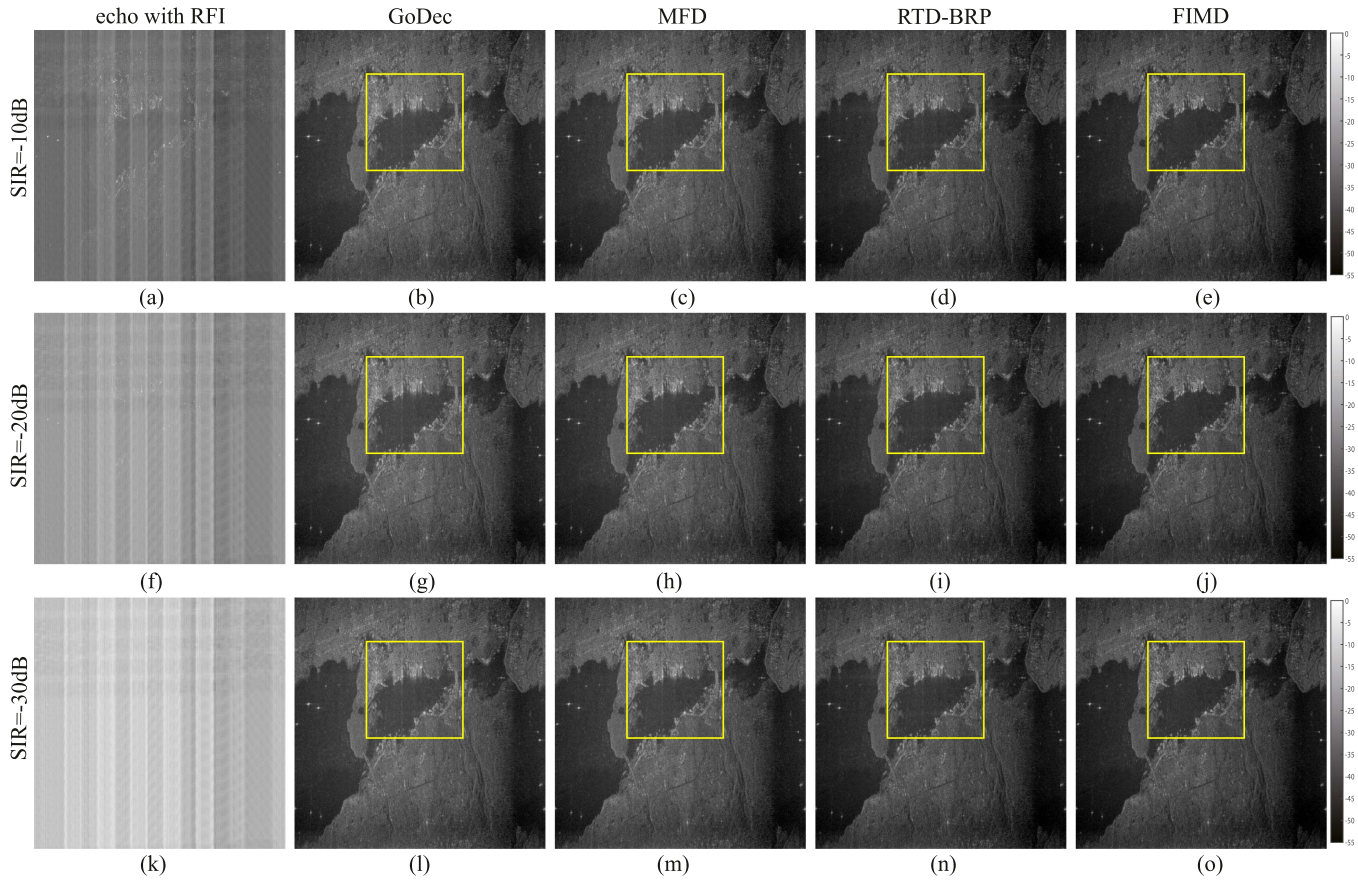

Fig. 4. Interference suppression results of four algorithms with SIR $= -10$ dB, SIR $= -20$ dB, and SIR $= -30$ dB.

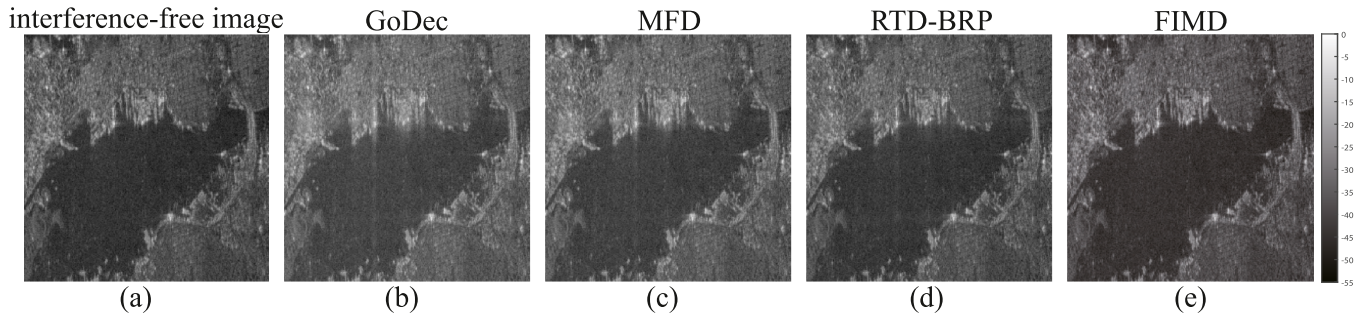

Fig. 5. Enlarged box image.

incomplete RFI suppression. Consequently, the resulting images suffer from poor contrast and lack distinct texture details. The FIMD algorithm demonstrates an excellent performance, intuitively showing that RFI is removed and achieving high-quality image restoration.

In order to provide a more detailed description of the suppression performance of the four algorithms, we locally magnify the scenes indicated by yellow color boxes in Fig. 4(g)–(j) under the condition of SIR $= -20$ dB. The scenes correspond to Fig. 5(b)–(e), and (a) represent the original interference-free images within the same region.

We observed that in Fig. 5, compared with (a), the occurrence of useful signal loss in (b) was attributed to the lack of sparse regularization protection in GoDec during the separation of sparse and low-rank signals. This resulted in some useful signals being mistakenly treated as low-rank signals and separated together with the RFI matrix during iteration. In cases where low-power RFIs were aliased with useful signals, it became indistinguishable, leading to residual RFI after imaging. In addition, since GoDec employs a hard threshold algorithm for updating the sparse matrix, there is a possibility of phase distortion in the original data, which affects imaging quality

TABLE II
INTERFERENCE SOURCE SIMULATION PARAMETER SETTINGS

Source	Frequency	Band width	Pluse width	Type
SIN	5.2935 GHz	0.2504 MHz	60.395 μs	NBI
LFM	5.3065 GHz	3.5336 MHz	20.812 μs	WBI
2PSK	5.2989 GHz	2.7342 MHz	–	WBI
SFM	5.3175 GHz	5.5415 MHz	–	WBI

and results in poor image clarity. Fig. 5(c) is the imaging result of the MFD algorithm, and the original image is well restored. This method accelerates algorithm convergence by decomposing the matrix into two smaller matrices for solving the low-rank matrix and transforming large-scale matrix optimization into an optimization problem involving these two smaller matrices. Nevertheless, it should be noted that this approach relies on a strict sparse low-rank model, which may limit its applicability to scenarios with broadband interference or mixed mode interference. This is because such interferences do not exhibit strict low-rank characteristics, resulting in residual RFI in imaging results. The imaging result of the RTD-BRP algorithm (d) is presented. In comparison to GoDec, this algorithm employs a soft-threshold approach that is better suited for handling complex data, enabling effective preservation of phase information during sparse part updates. However, it should be noted that both RTD-BRP and MFD share similar limitations. Specifically, if the scene is intricate and does not strictly adhere to a "sparse+low rank" model, the algorithm's performance will be limited. Among the four algorithms compared, (e) exhibits the most effective performance in image restoration. Due to its utilization of a weight factor based on the F-norm, which effectively preserves strong scattering points and prevents their removal as interference signals. While also operating within the framework of a sparse low rank model, the FIMD algorithms employs the CUR algorithm for updating the low rank matrix by extracting varying numbers of rows and columns from the original data. This approach ensures preservation of the original matrix structure while maintaining data sparsity. It is also a direct low rank approximation of the original matrix. The imaging results accurately depict the target scene. In comparison to (b), (c), and (d), it is evident that the proposed algorithm exhibits a rich representation of detailed textures, closely resembling real images without interference.

Based on the simulation parameters outlined in Table II, four algorithms were compared for RSIR, SSIM, and running time across varying SIRs. The numerical results are presented in Table III. Evaluation of interference suppression ability under different SIRs revealed that the proposed method outperformed comparison other three algorithms. The running time of the FIMD algorithm is longer than that of the MFD and RTD-BRP algorithms, primarily due to two factors. First, there is a need for sorting the weight coefficients each time the weight factors of the F-norm are constructed, resulting in increased computational time. The second reason is that in order to more accurately simulate the real and complex electromagnetic environment, a variety of narrowband and broadband interferences have been incorporated into this scenario, rendering it unsuitable as an ideal

TABLE III
NUMERICAL ANALYSIS RESULTS

	Method	GoDec	MFD	RTD-BRP	FIMD
SIR=−10	RSIR	20.95	23.49	30.05	**46.11**
	SSIM	0.9881	0.9943	0.9913	**0.9994**
	TIME	4.02	0.81	**0.17**	2.47
SIR=−20	RSIR	20.95	23.49	31.51	**46.23**
	SSIM	0.9897	0.9942	0.9914	**0.9994**
	TIME	4.03	0.78	**0.17**	2.52
SIR=−30	RSIR	20.94	23.50	31.55	**46.14**
	SSIM	0.9896	0.9942	0.9914	**0.9995**
	TIME	4.02	0.77	**0.16**	2.51

The best results for each indicator are highlighted in bold.

low rank scene. Although RSVD is employed instead of SVD for low-rank problem solving, leading to accelerated algorithm convergence, it necessitates the extraction of more rows and columns in complex scenes, resulting in an overall increase in computational time. Numerical analysis results demonstrate the proposed algorithm's strong suppression capability and robustness.

B. *Sentinel-1 SLC Image With RFI Interference*

The proposed method was employed in this section to experimentally validate S-1 IW images containing real interference. Fig. 6(a) illustrates the raw SLC image, acquired by Sentinel 1 near the Persian Gulf Sea on January 5, 2022, with azimuth and range resolutions of 20 m and 3 m, respectively. The data identifier is S1A_IW_SLC_1SDV_20220105T142412_20220105T142439_041327_04E9C3_6E3C. The data size is $21\,743 \times 13\,446$ pixels. In order to facilitate visualization, we compressed the data after processing. Figs. 6 and 7 are the compressed data. The partial zone in Fig. 6(a) exhibits severe interference artifacts, which obscure a portion of the sea surface. To enhance overall operational efficiency, we employ interference suppression on single sub-bands containing RFI and then concatenate the sub-bands. In Fig. 6(b), the effectiveness of suppression is demonstrated with con $= 200$, resulting in the removal of most artifacts and revealing a pristine sea surface with clear image structure. The suppressed RFI artifact photo is depicted in Fig. 6(c). The results demonstrate that the proposed algorithm effectively eliminates radiation artifacts caused by RFI in the image domain, while minimizing loss of useful signal. In order to facilitate a more comprehensive performance comparison of the proposed algorithm, we employed the BSF [7] as the contrast algorithm using identical data settings. Specifically, with block_len $= 200 \times 200$ and $k = 5$, Fig. 7 demonstrates the suppression effect achieved. Fig. 7(a) represents the original image, (b) showcases the outcome after applying the BSF algorithm for suppression, while (c) exhibits the extracted artifacts by means of this algorithm. It can be seen from Fig. 7(c) that the BSF algorithm can also suppress RFI and obtain

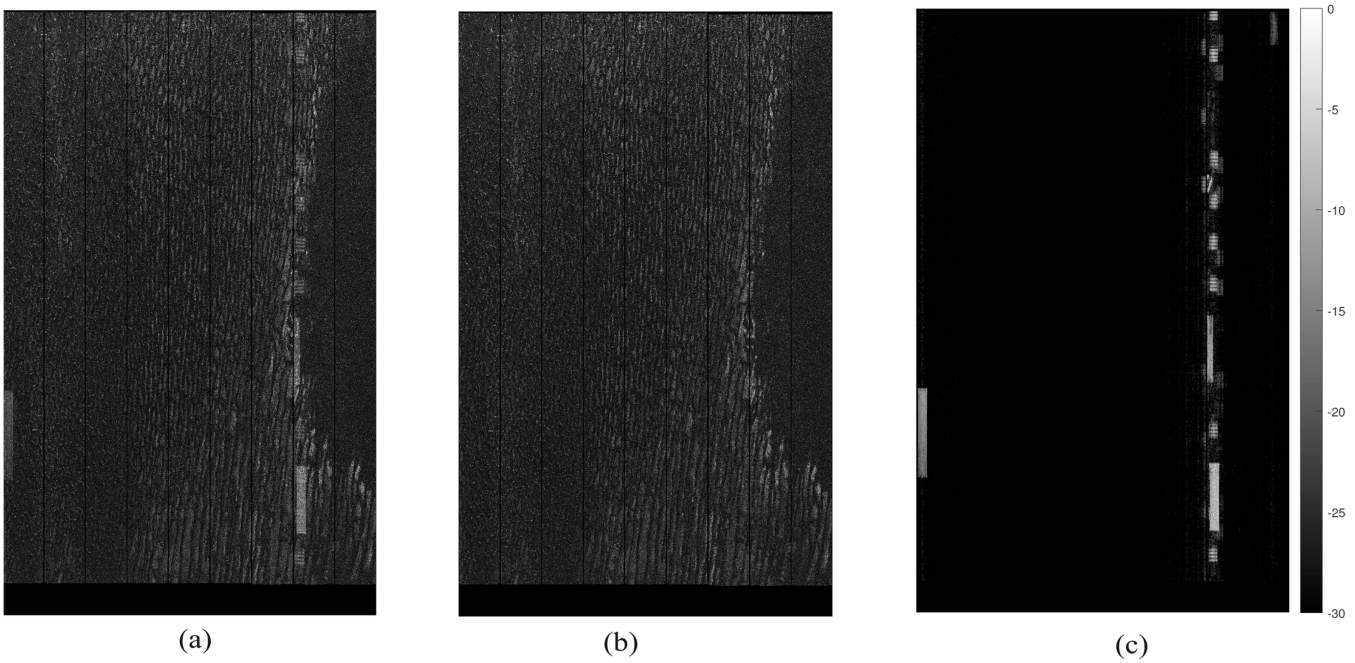

Fig. 6. FIMD algorithm suppression results. (a) SLC image with RFI. (b) Image suppressed by FIMD algorithm. (c) RFI image.

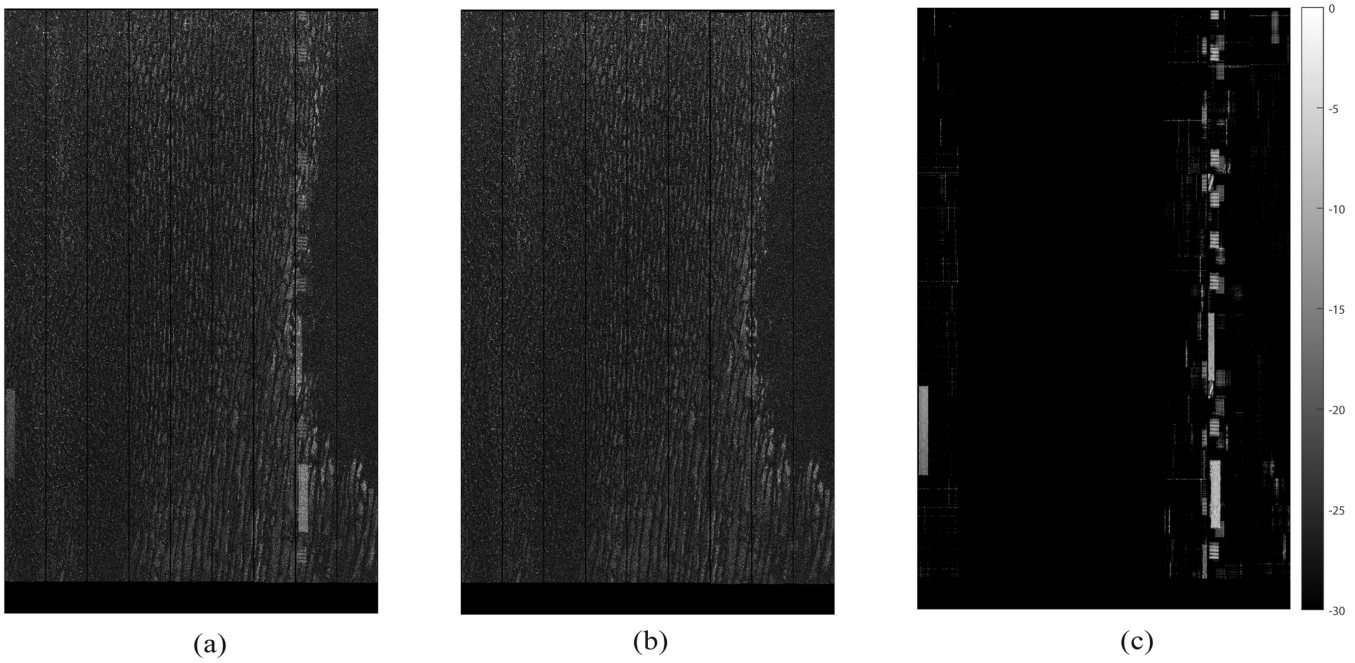

Fig. 7. BSF algorithm suppression results. (a) SLC image with RFI. (b) Image suppressed by BSF algorithm. (c) RFI image.

a clean image without interference. The following presents a qualitative analysis of the two algorithms. Comparatively, the proposed algorithm exhibits superior interference suppression and minimal loss of useful signals in contrast to the BSF algorithm. While removing RFI artifacts, BSF algorithm eliminates some useful signals as RFI. This is due to the partial correlation between some useful signal subspaces in the matrix and the estimated low-rank interference subspaces, which results in the amplitude reduction after interference suppression, and some useful signals are projected into the interference subspaces, resulting in the loss of useful signals.

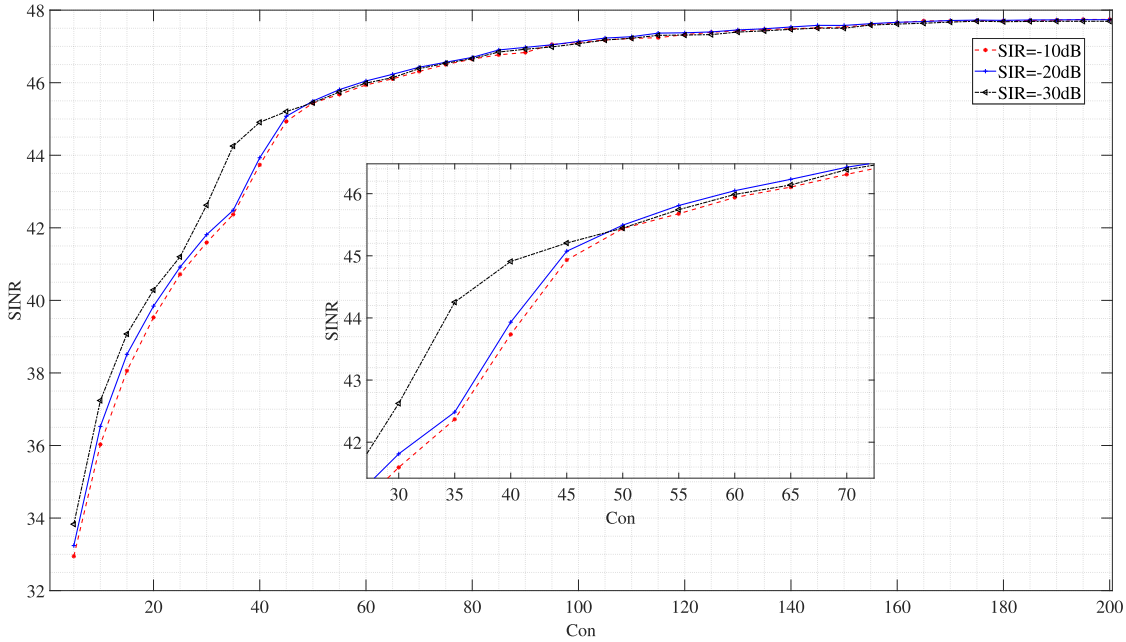

Fig. 8. Relationship between sampling parameters and SINR.

C. Performance Analysis of the Proposed Algorithm

Analyzing the influence of sampling row quantity on the efficacy of the proposed algorithm, Fig. 8 illustrates the correlation between sampling parameters and SINR. Initially, we present the relationship between abscissa sampling parameters and sample quantity (SQ)

$$\mathrm{SQ} = \mathrm{Con} \times r \times \log(m) \tag{23}$$

where Con represents the sampling parameter and SQ denotes the number of rows and columns sampled from the actual matrix. When SIR $= -10$ dB, SIR $= -20$ dB, and SIR $= -30$ dB, set the Con step to 5 for iteration. When Con $= 45$, the proposed algorithm is essentially immune to the influence of SIR. The algorithm consistently performs near SINR $= 47.62$ dB is achieved when Con $= 160$. While a maximum SINR $= 47.69$ dB as the number of sampled rows and columns increases, reaching its limit. The primary cause of this issue lies in two factors. First, the performance of CUR decomposition restricts the proposed algorithm, resulting in reconstruction errors during each iteration. Second, by sampling from the entire echo matrix, valuable signals may be lost in areas without interference due to variations in echo amplitude. Therefore, it is advisable to construct a more suitable weighting factor based on prior information to minimize reconstruction errors or preprocess the echo matrix using the FIMD algorithm specifically targeting areas with interference.

When the RFI power of SAR is high, both the conventional method and the proposed approach effectively mitigate RFI, as elaborated in Section IV-A. The corresponding numerical analysis is presented in Table III. In scenarios where SIR is high, indicating relatively low energy of RFI, aliasing occurs between RFI and useful signals making their separation challenging. In this section, we investigate the lower limit of the proposed

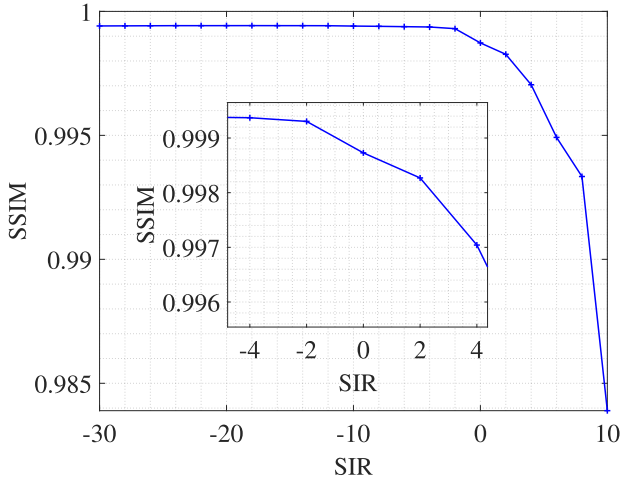

Fig. 9. Relationship between SIR and SSIM.

algorithm. With SSIM $= 0.99$ as the benchmark, indicating that the image restoration similarity reaches 99%, we conducted the following experimental design. The SIR ranges from -30 dB to 10 dB with a step size of 2 dB. The relationship between the degree of image recovery and SIR is illustrated in Fig. 9. It can be observed that at low SIR values, our proposed algorithm achieves a high and stable image recovery degree, reaching SSIM $= 0.9994$. However, as the SIR increases, a turning point occurs at SIR $= -2$ dB where the performance of our proposed algorithm starts to decline gradually. At SIR $= 8$ dB, SSIM drops to 0.9933 before plummeting further; interestingly, it is worth noting that the lower bound of SSIM $= 0.99$ lies between SIR $= 8$ dB and SIR $= 9$ dB. The proposed algorithm can successfully recover the original image with a similarity

TABLE IV
COMPUTATIONAL COMPLEXITY OF THE PROPOSED ALGORITHM AND THE COMPARISON ALGORITHM

algorithm	computational complexity
GoDec	$\mathcal{O}\left(r^2(2N+r)+3MNr)\right)$
MFD	$\mathcal{O}\left(mnd+md^2+2mn)\right)$
RTD-BRP	$\mathcal{O}\left(r^3+2Lr^2+2ML)\right)$
FIMD	$\mathcal{O}\left(n\log(n)+IJ\log(r)+(I+J)r^2+mn)\right)$

exceeding 99% when SIR ≤ 8, which satisfies the requirements of most practical applications. Blindly increasing the SIR value is not meaningful since certain anti-interference capabilities are already incorporated in steps like pulse compression during the imaging process. When SIR $= 10$ dB, RFI artifacts can no longer be seen from imaging results.

D. Computational Complexity Analysis

The proposed algorithm iterates sequentially under the alternating projection framework, where descending sorting is required when designing weight factors based on the F-norm, and the required complexity is $\mathcal{O}(n\log(n)))$, when the mixing submatrix $\boldsymbol{U}$ is updated by the CUR algorithm, SVD decomposition will cost at least $\mathcal{O}(\min(m^2\times n, n^2\times m))$. By employing RSVD instead of SVD, the computational complexity is significantly reduced to $\mathcal{O}(IJ\log(r)+(I+J)r^2))$. When the echo matrix is large, the time complexity of RSVD is much smaller than that of SVD, and the soft-threshold algorithm needs to update useful signals $\mathcal{O}(mn))$. Then, the total time complexity of the proposed algorithm $\mathcal{O}(n\log(n)+IJ\log(r)+(I+J)r^2+mn))$. Table IV shows the computational complexity of the proposed algorithm and the comparison algorithm.

V. DISCUSSION

The numerical experiments and analysis in Section IV show that the proposed algorithm is less affected by SIR, and shows better suppression ability to MRFI and robustness of the algorithm. However, when dealing with actual interference data, useful signals still appear to be eliminated, indicating that the performance of the proposed algorithm will decline in the scenario of large-area strong scattering points gathering, because the proposed method is limited by the CUR algorithm and the interference of strong scattering points, which cannot guarantee that the low-rank matrix obtained is the best low-rank of the original matrix. In addition, the main time-consuming steps of FIMD algorithm have been analyzed in the previous part. In the next step, we consider using approximate estimation of F-norm weight factors of rows and columns instead of accurate calculation, so as to avoid the time loss caused by weight factor ranking in iteration and reduce the computational complexity of the algorithm. Finally, we point out that the proposed algorithm still exhibits excellent RFI suppression capability in complex electromagnetic scenarios. Because of its simplicity, generality, and flexibility, it is hoped to become a powerful tool for remote sensing scholars to obtain clean SAR data in advanced SAR application scenarios.

VI. CONCLUSION

In this article, we propose an iterative matrix factorization algorithm based on the F-norm. The CUR decomposition is employed to update the low-rank matrix, while the soft-threshold algorithm is utilized for updating the sparse matrix during the iterative process, and the SAR echo matrix is low-rank reconstructed, which effectively suppresses MRFI. Furthermore, based on the distinct distribution characteristics of interference signals and strong scatterers in the echo domain. We propose a method using a row/column weighting factor constructed by the F-norm to effectively prevent useful signals from being eliminated as interference. In addition, to enhance algorithm convergence speed, we employ RSVD instead of SVD algorithm. The proposed algorithm effectively preserves the structural and target characteristics of the original echo matrix, while simultaneously analyzing the limitations of the algorithm. Numerical experiments conducted under different SIRs demonstrate that the algorithm we propose demonstrates robustness, exhibits superior performance in suppressing RFI, remains unaffected by various types of interference (including narrowband, broadband, and mixed interference), and can be effectively applied to both L0-raw products and L1-SLC products.

REFERENCES

[1] N. Li, Z. Lv, Z. Guo, and J. Zhao, "Time-domain notch filtering method for pulse RFI mitigation in synthetic aperture radar," *IEEE Geosc. Remote Sens. Lett.*, vol. 19, May 2022, Art. no. 4013805.

[2] J. Shen, B. Han, Z. Pan, G. Li, Y. Hu, and C. Ding, "Learning time-frequency information with prior for SAR radio frequency interference suppression," *IEEE Trans. Geosci. Remote Sens.*, vol. 60, Jan. 2022, Art. no. 5239716.

[3] Y. Li, Z. Zhou, and C. Fan, "Time-frequency analysis of RFI data and interference suppression using match pursuit algorithm," in *Proc. 18th Int. Radar Symp.*, 2017, pp. 1–5.

[4] W. Xu, W. Xing, C. Fang, P. Huang, and W. Tan, "RFI suppression based on linear prediction in synthetic aperture radar data," *IEEE Geosc. Remote Sens. Lett.*, vol. 18, no. 12, pp. 2127–2131, Dec. 2021.

[5] W. Peng, Y. Lin, Z. Yong-Sheng, D. Zhen, W. Min, and D. Siyao, "A modified notch filter for suppressing radio-frequency-interference in P-band SAR data," in *Proc. IEEE Int. Geosci. Remote Sens. Symp.*, 2016, pp. 4988–4991.

[6] F. Zhou and M. Tao, "Research on methods for narrow-band interference suppression in synthetic aperture radar data," *IEEE J. Sel. Topics Appl. Earth Observ. Remote Sens.*, vol. 8, no. 7, pp. 3476–3485, Jul. 2015.

[7] H. Yang, K. Li, J. Li, Y. Du, and J. Yang, "BSF: Block subspace filter for removing narrowband and wideband radio interference artifacts in single-look complex SAR images," *IEEE Trans. Geosci. Remote Sens.*, vol. 60, Jul. 2022, Art. no. 5211916.

[8] J. Feng, H. Zheng, Y. Deng, and D. Gao, "Application of subband spectral cancellation for SAR narrow-band interference suppression," *IEEE Geosc. Remote Sens. Lett.*, vol. 9, no. 2, pp. 190–193, Mar. 2012.

[9] B. Chen, Z. Lv, P. Lu, G. Shu, Y. Huang, and N. Li, "Extension and evaluation of SSC for removing wideband RFI in SLC SAR images," *Remote Sens.*, vol. 14, no. 17, Sep. 2022, Art. no. 4294.

[10] H. Yang, Y. He, Y. Du, T. Zhang, J. Yin, and J. Yang, "Two-dimensional spectral analysis filter for removal of LFM radar interference in spaceborne SAR imagery," *IEEE Trans. Geosci. Remote Sens.*, vol. 60, Dec. 2022, Art. no. 5219016.

[11] L. Nguyen and M. Soumekh, "Suppression of radio frequency interference (RFI) for synchronous impulse reconstruction ultra-wideband radar," *Proc. SPIE*, vol. 5808, pp. 178–184, 2005.

[12] T. R. Miller, J. W. Mccorkle, and L. C. Potter, "Near-least-squares radio frequency interference suppression," *Defense, Secur., Sens.*, vol. 1, pp. 72–83, 1995.

[13] M. Braunstein, J. M. Ralston, and D. A. Sparrow, "Signal processing approaches to radio frequency interference (RFI) suppression," in *Proc. SPIE*, vol. 2230, 1994, pp. 1–20.
[14] F. Zhou, M. Xing, X. Bai, G. Sun, and Z. Bao, "Narrow-band interference suppression for SAR based on complex empirical mode decomposition," *IEEE Geosc. Remote Sens. Lett.*, vol. 6, no. 3, pp. 423–427, Jul. 2009.
[15] A. Potis, N. Uzunoglou, P. Frangos, R. Horn, and K. Lamprecht, "Analysis of p-band synthetic aperture radar for airborne and spaceborne applications," *Comput. Eng.*, vol. 1, pp. 16–18, Oct. 2000.
[16] H. Liu, L. Gan, D. Li, and T.-K. Truong, "RFI suppression based on atomic norm minimization in SAR signal recovery," in *Proc. IEEE Int. Conf. Image Process.*, 2019, pp. 2040–2044.
[17] X. Lu et al., "Radio frequency interference suppression for SAR via block sparse Bayesian learning," *IEEE J. Sel. Topics Appl. Earth Observ. Remote Sens.*, vol. 11, no. 12, pp. 4835–4847, Dec. 2018.
[18] F. Hu, L. Wu, J. Li, X. Peng, D. Zhu, and Y. Cheng, "RFI localization in synthetic aperture interferometric radiometers based on sparse Bayesian inference (vol 38, pg 5502, 2017)," *Int. J. Remote Sens.*, vol. 38, no. 20, pp. 5502–5523, 2017.
[19] J. Su, H. Tao, M. Tao, L. Wang, and J. Xie, "Narrow-band interference suppression via RPCA-based signal separation in time-frequency domain," *IEEE J. Sel. Topics Appl. Earth Observ. Remote Sens.*, vol. 10, no. 11, pp. 5016–5025, Nov. 2017.
[20] H. Yang, C. Chen, S. Chen, F. Xi, and Z. Liu, "A dictionary-based SAR RFI suppression method via robust PCA and chirp scaling algorithm," *IEEE Geosc. Remote Sens. Lett.*, vol. 18, no. 7, pp. 1229–1233, Jul. 2021.
[21] Y. Huang, Z. Chen, C. Wen, J. Li, X.-G. Xia, and W. Hong, "An efficient radio frequency interference mitigation algorithm in real synthetic aperture radar data," *IEEE Trans. Geosci. Remote Sens.*, vol. 60, Mar. 2022, Art. no. 5224912.
[22] Y. Huang, G. Liao, Z. Zhang, Y. Xiang, J. Li, and A. Nehorai, "Fast narrowband RFI suppression algorithms for SAR systems via matrix-factorization techniques," *IEEE Trans. Geosci. Remote Sens.*, vol. 57, no. 1, pp. 250–262, Jan. 2019.
[23] Y. Huang, G. Liao, J. Xu, and J. Li, "Narrowband RFI suppression for SAR system via efficient parameter-free decomposition algorithm," *IEEE Trans. Geosci. Remote Sens.*, vol. 56, no. 6, pp. 3311–3322, Jun. 2018.
[24] Y. Huang, L. Zhang, J. Li, W. Hong, and A. Nehorai, "A novel tensor technique for simultaneous narrowband and wideband interference suppression on single-channel SAR system," *IEEE Trans. Geosci. Remote Sens.*, vol. 57, no. 12, pp. 9575–9588, Dec. 2019.
[25] Y. Huang, L. Zhang, J. Li, Z. Chen, and X. Yang, "Reweighted tensor factorization method for SAR narrowband and wideband interference mitigation using smoothing multiview tensor model," *IEEE Trans. Geosci. Remote Sens.*, vol. 58, no. 5, pp. 3298–3313, May 2020.
[26] P. R. Foster, "Introduction to ultra-wideband radar systems," in *Ultra Wideband Wireless Communications.* Boca Raton, FL, USA: CRC Press, 1995.
[27] Z. Tang, Y. Deng, and H. Zheng, "RFI suppression for SAR via a dictionary-based nonconvex low-rank minimization framework and its adaptive implementation," *Remote Sens.*, vol. 14, no. 3, pp. 1–31, Feb. 2022.
[28] H. Zhang, Y. Huang, J. Li, Z. Chen, L. Cai, and W. Hong, "Time-varying RFI mitigation for SAR systems via graph Laplacian clustering techniques," *IEEE Geosc. Remote Sens. Lett.*, vol. 19, Mar. 2022, Art. no. 4010805.
[29] Y. Huang, L. Lan, Y. Xin, J. Chen, Y. Liu, and J. Li, "Narrowband RFI suppression on high-resolution wide-swath SAR systems via low-rank recovery," in *Proc. IEEE Int. Geosci. Remote Sens. Symp.*, 2022, pp. 5137–5140.
[30] Y. Huang, G. Liao, Z. Zhang, Y. Xiang, J. Li, and A. Nehorai, "Fast narrowband RFI suppression algorithms for SAR systems via matrix-factorization techniques," *IEEE Trans. Geosci. Remote Sens.*, vol. 57, no. 1, pp. 250–262, Jan. 2019.
[31] A. S. Goreinov, E. E. Tyrtyshnikov, and L. N. Zamarashkin, "A theory of pseudoskeleton approximations," *Linear Algebr. Appl.*, vol. 261, no. 1, pp. 1–21, 1997.
[32] C. Chen, M. Gu, Z. Zhang, W. Zhang, and Y. Yu, "Efficient spectrum-revealing CUR matrix decomposition," in *Proc. Int. Conf. Artif. Intell. Statist.*, 2020, vol. 108, pp. 26–28.
[33] K. Hamm and L. Huang, "Perspectives on cur decompositions," *Appl. Comput. Harmon. Anal.*, vol. 48, no. 3, pp. 1088–1099, May 2020.
[34] H. Q. Cai, K. Hamm, L. Huang, J. Li, and T. Wang, "Rapid robust principal component analysis: CUR accelerated inexact low rank estimation," *IEEE Signal Process. Lett.*, vol. 28, pp. 116–120, Dec. 2021.
[35] Y. Ding, W. Fan, Z. Zhang, F. Zhou, and B. Lu, "Radio frequency interference mitigation for synthetic aperture radar based on the time-frequency constraint joint low-rank and sparsity properties," *Remote Sens.*, vol. 14, no. 3, pp. 1–30, Feb. 2022.
[36] L. Min, A. Wu, X. Fan, F. Li, and J. Li, "Dim and small target detection with a combined new norm and self-attention mechanism of low-rank sparse inversion," *Sensors*, vol. 23, no. 16, Aug. 2023.
[37] T. Zhou and D. Tao, "Godec: Randomized lowrank & sparse matrix decomposition in noisy case," in *Proc. Int. Conf. Mach. Learn.*, 2011, pp. 1–8.

Qiang Guo received the B.S., M.S., and Ph.D. degrees in information and communication engineering from Harbin Engineering University, Harbin, China, in 1994, 2003, and 2007, respectively.

He has been a Professor with Harbin Engineering University since 2009. His research interests include radio-frequency interference in synthetic aperture radar and target comprehensive identification.

Dr. Guo is currently a Foreign member of the Ukrainian Academy of Engineering, Review Expert of the Science and Technology Commission of the Military Commission, the National Natural Science Foundation of China and Technology Department evaluation expert, and the Chinese Institute of Electronics Science and Technology Award evaluation expert.

Yuhang Tian was born in Zhangjiakou, Hebei Province, China in 1995. He received the B.S. degree in electronic information science and technology from Hebei Agricultural University, Baoding, China, where he is currently working toward the Ph.D. degree in information and communication engineering with the Harbin Engineering University of Information and Communication Engineering.

His research interests include radio-frequency interference in synthetic aperture radar and radar signal processing.

Liangang Qi was born in Hebei, China, in 1990. He received the B.S. and Ph.D. degrees in information and communication engineering from Harbin Engineering University, Harbin, China, in 2013 and 2018, respectively.

He was a Postdoctoral Fellow with the Sichuan Key Laboratory of Agile Intelligent Computing, Tenth Research Institute of China Electronics Technology Group Corporation, Sichuan, China. He has been a Lecturer with Harbin Engineering University, since 2018. His research interests include satellite navigation antijamming, radar antijamming, and radar signal processing.

Yani Wang was born in Tangshan Hebei, China, in 1991. She is currently working toward the Ph.D. degree in information and communication engineering with Harbin Engineering University, Harbin, China.

Her research interests include antenna array synthesis and sparse signal processing.

Daren Li was born in Haerbin, Heilongjiang Province, China, in 1990. He received the M.S. degree in shipbuilding and ocean engineering from the College of Shipbuilding Engineering, Harbin Engineering University, Harbin, China, where he is currently working toward the Ph.D. degree in information and communication engineering with Harbin Engineering University of Information and Communication Engineering.

His research interests include radar signal processing and target comprehensive identification.

Mykola Kaliuzhnyi received the B.S. and Ph.D. degrees in radio engineering from the Saratov State University of the Soviet Union, Soviet Union, Saratov Oblast, Russia, in 1971, and Former Soviet Communication Air Force Engineering Academy, Soviet Union, Kharkiv, Ukraine, in 1987, respectively.

Since 2008, he has been working at Kharkiv National University of Radio and Electronics, Ukraine, where he currently serves as Professor and Director of the Scientific Laboratory of Advanced Problems. He has been appointed as a visiting Professor at Harbin Engineering University since 2017. His research interests include radio frequency monitoring, radar signal processing and radio communication.